

Plate 10.2. Two left-hand columns: $-b_1/a_1$ (in %) versus scattering angle and effective size parameter for polydisperse randomly oriented spheroids with various axis ratios and a fixed relative refractive index $m = 1.53 + i0.008$. The distribution of surface-equivalent-sphere radii is given by Eq. (5.246) with $\alpha = -3$ and $v_{\text{eff}} = 0.1$. Two right-hand columns: as in the two left-hand columns, but for the ratio of the phase function α_1 for randomly oriented polydisperse spheroids and that for surface-equivalent spheres.

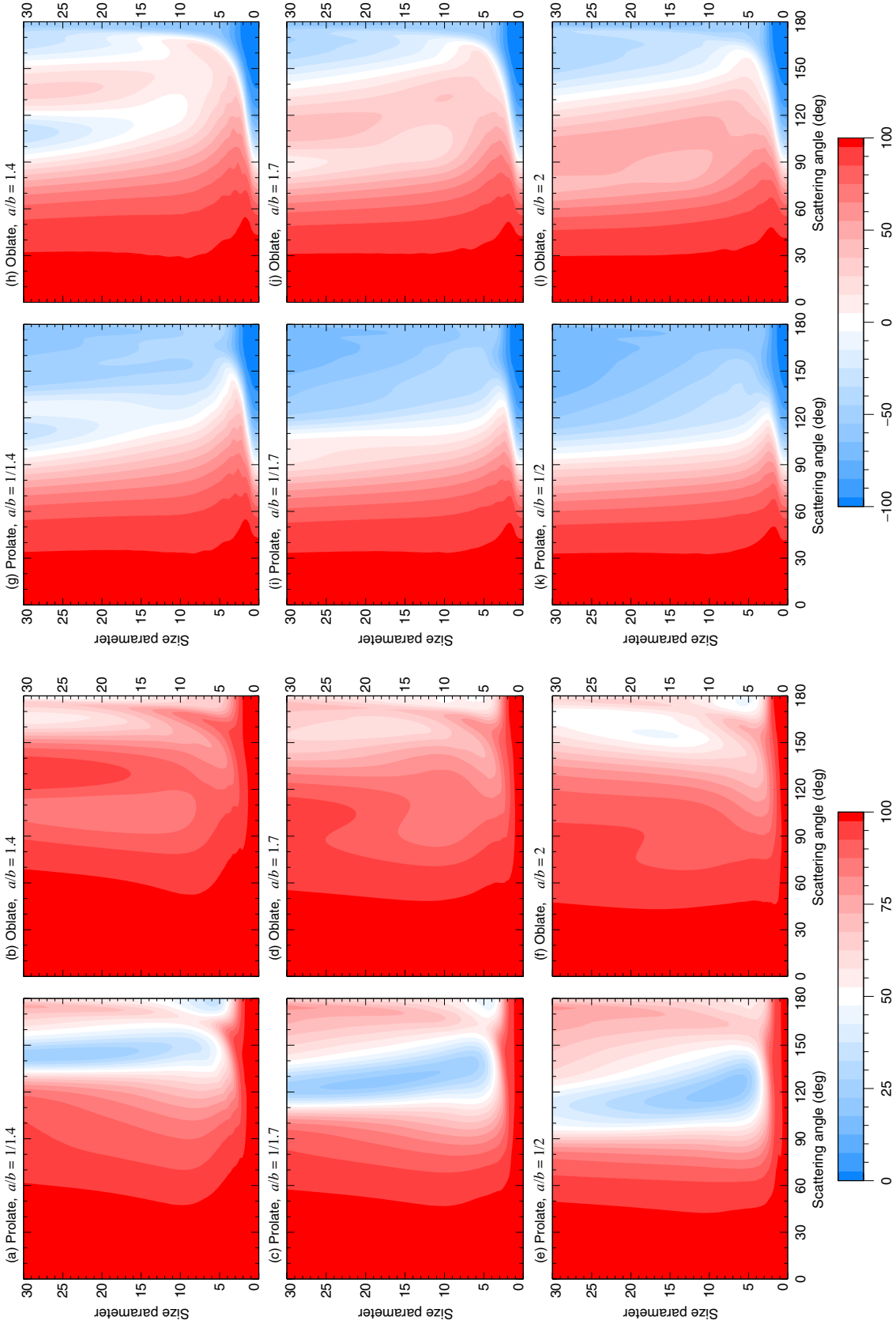


Plate 10.3. As in the two left-hand columns of Plate 10.2, but for a_2/a_1 (the two left-hand columns) and a_3/a_1 (the two right-hand columns).

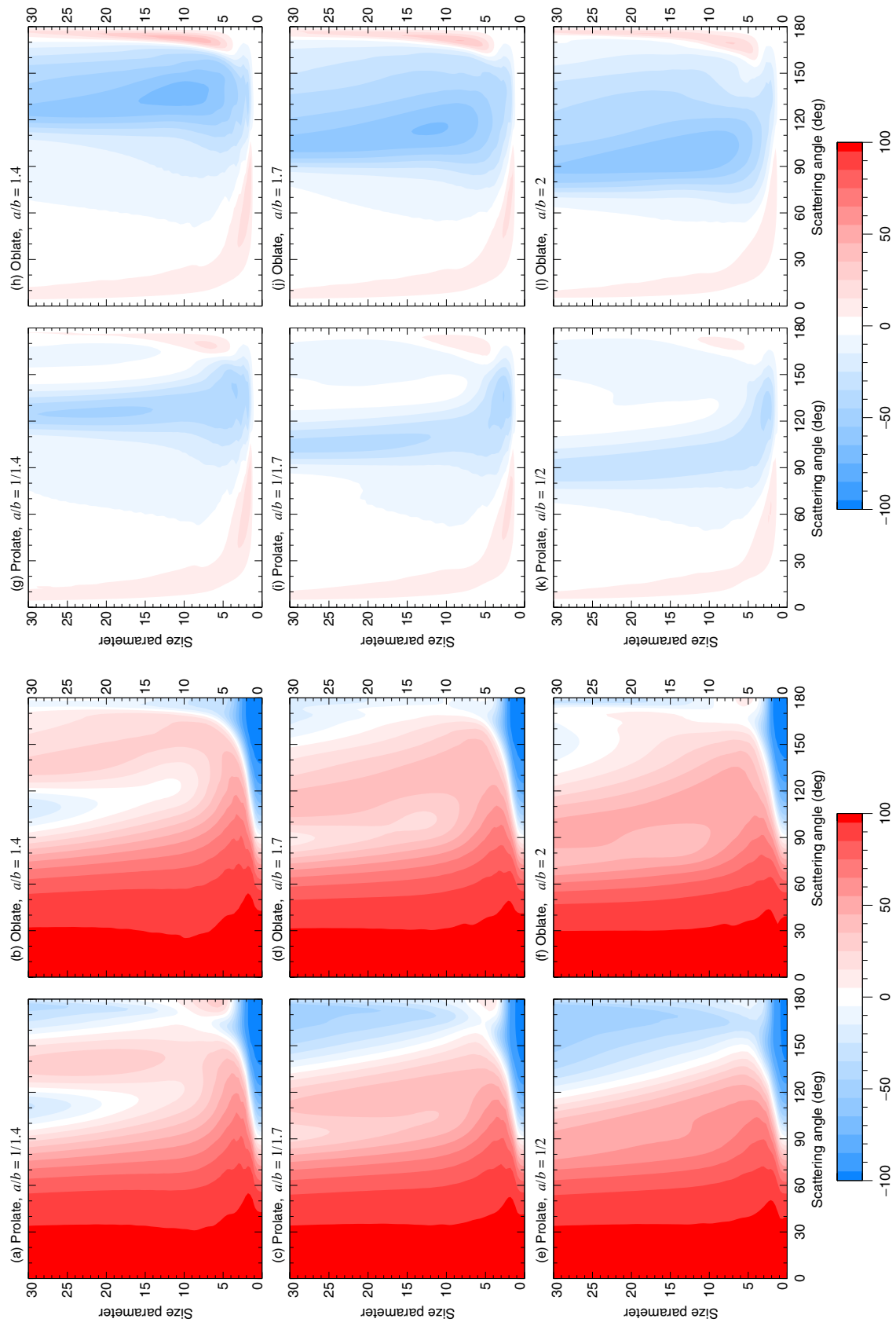


Plate 10.4. As in the two left columns of Plate 10.2, but for a_4/a_1 (the two left-hand columns) and b_2/a_1 (the two right-hand columns).

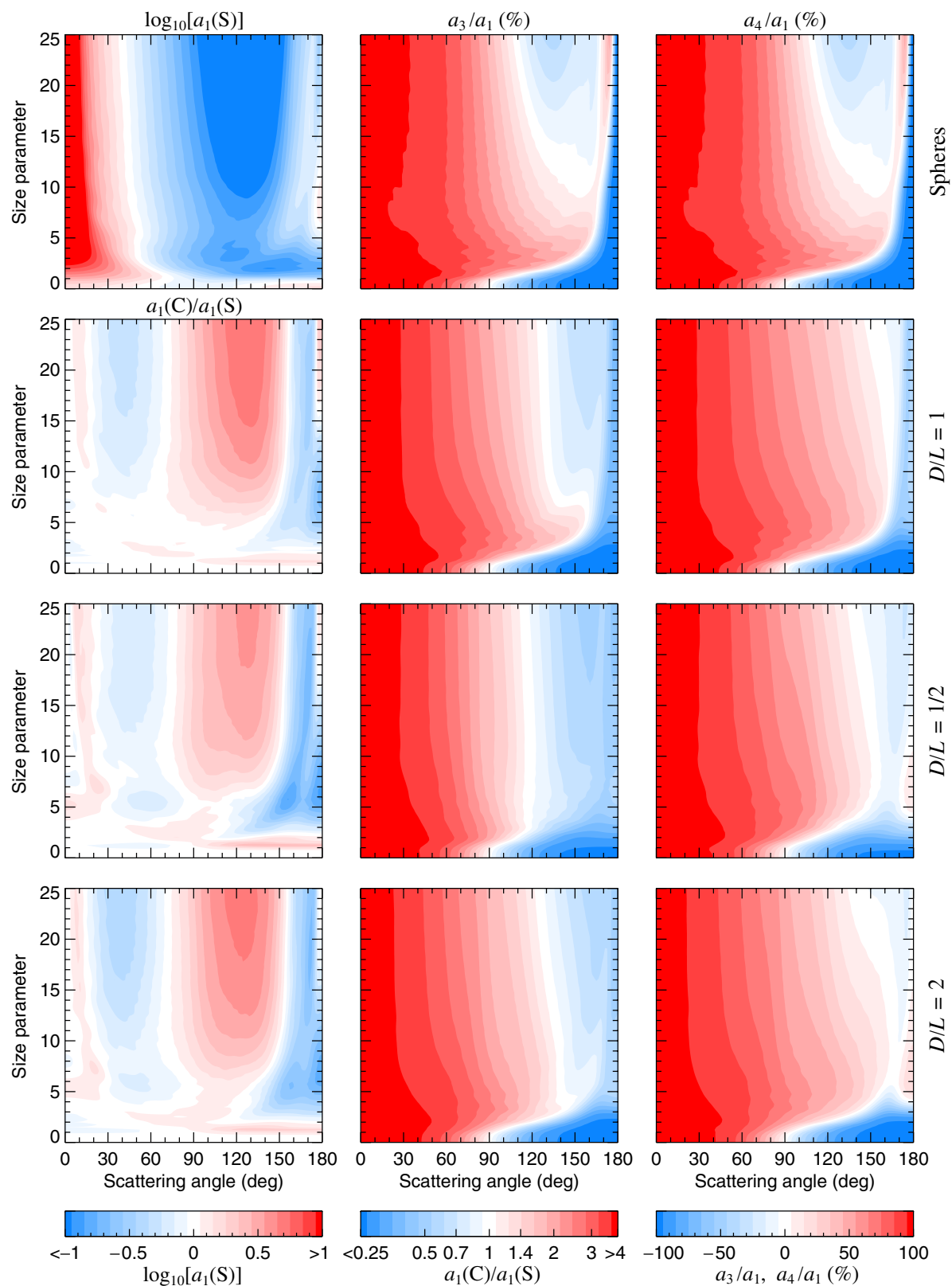


Plate 10.5. The top left panel shows the logarithm of the phase function versus scattering angle and effective size parameter for polydisperse spheres. The three lower diagrams in the left-hand column show the ratio of the phase function $a_1(C)$ for polydisperse randomly oriented cylinders with $D/L = 1, 1/2,$ and 2 and the phase function $a_1(S)$ for surface-equivalent spheres. The middle and right-hand columns show a_3/a_1 and a_4/a_1 for spheres (top panels) and for surface-equivalent cylinders (lower three pairs of panels). Each diagram is quantified by the corresponding color bar at the bottom of the plate. All particles have the same relative refractive index, $1.53 + i0.008$. The distribution of surface-equivalent-sphere radii is given by Eq. (5.246) with $\alpha = -3$ and $v_{\text{eff}} = 0.1$.

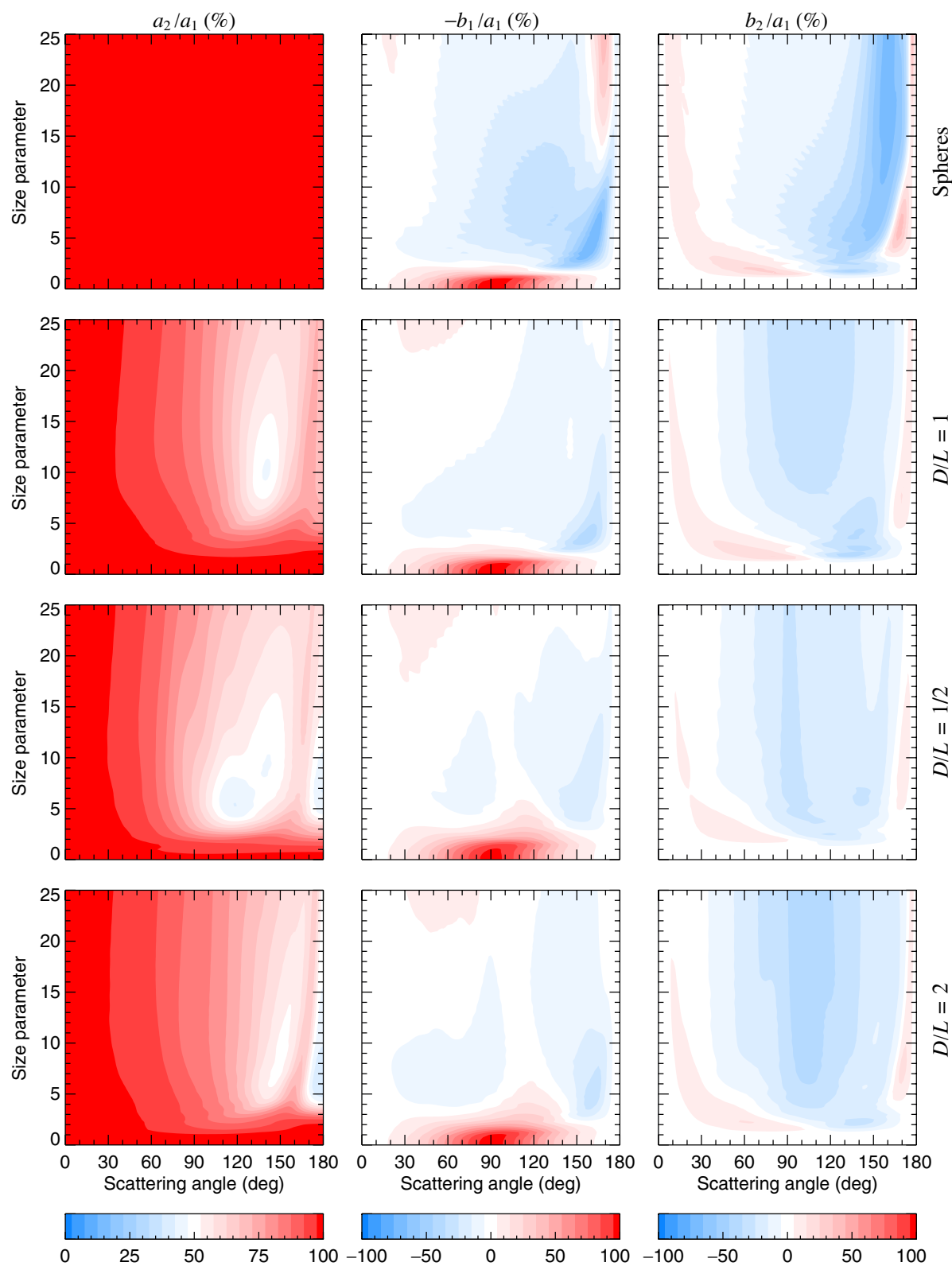


Plate 10.6. The ratios a_2/a_1 , $-b_1/a_1$, and b_2/a_1 for polydisperse spheres and for surface-equivalent randomly oriented cylinders with $D/L = 1, 1/2$, and 2 . The diagrams in each column are quantified using the color bar below the column. All particles have the same relative refractive index, $1.53 + i0.008$. The distribution of surface-equivalent-sphere radii is given by Eq. (5.246) with $\alpha = -3$ and $v_{\text{eff}} = 0.1$.

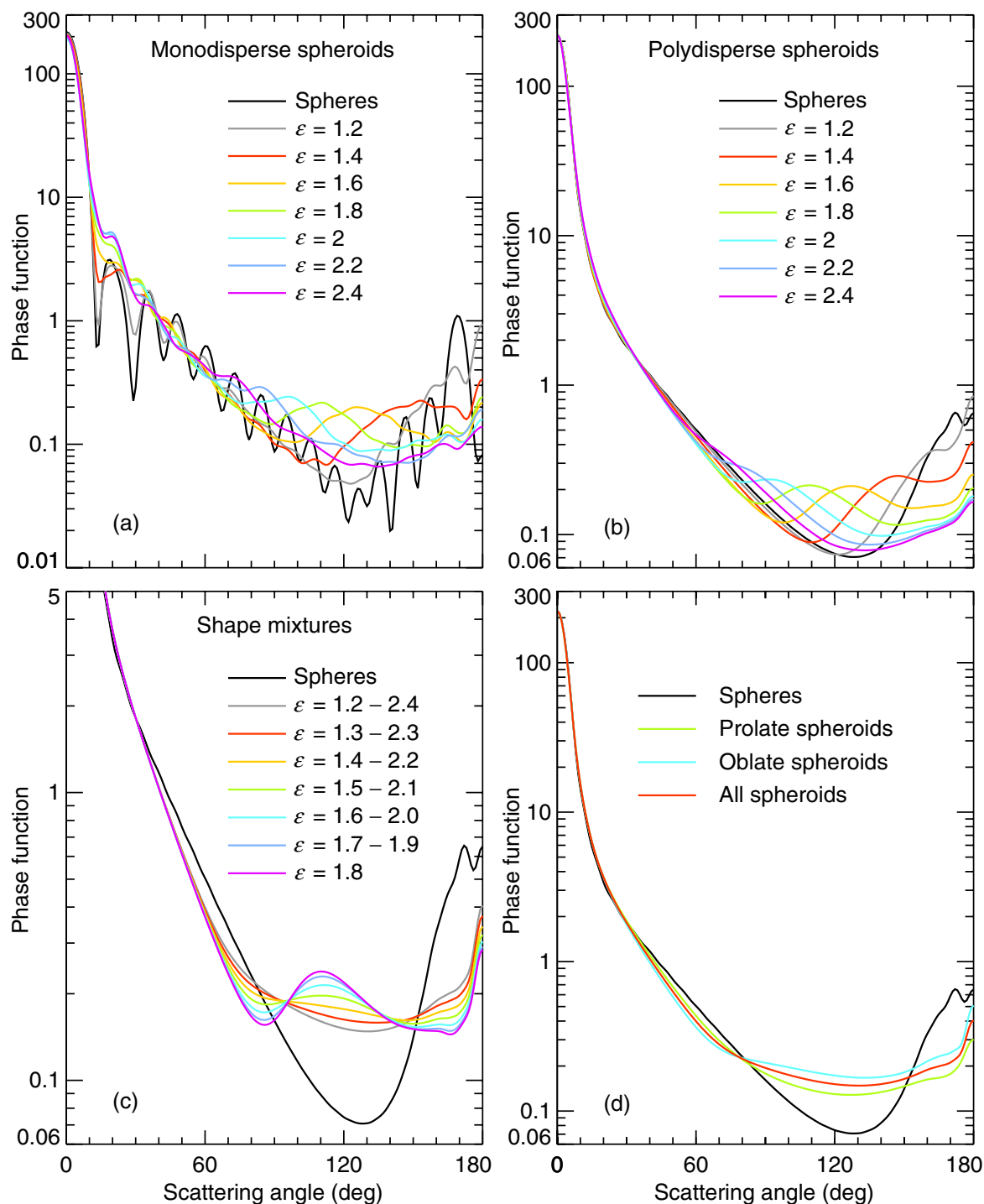


Plate 10.7. *T*-matrix computations of phase function versus scattering angle for monodisperse and polydisperse spheres and randomly oriented spheroids with a relative refractive index $1.53 + i0.008$ at a wavelength 443 nm . Panel (a) shows results for a monodisperse sphere with a radius $1.163 \text{ }\mu\text{m}$ and for surface-equivalent prolate spheroids with aspect ratios ranging from 1.2 to 2.4. Panel (b) shows similar computations but for a log normal size distribution with an effective radius $1.163 \text{ }\mu\text{m}$ and an effective variance 0.168. Panel (c) demonstrates the effect of using a spheroid aspect-ratio distribution of finite width; it shows the ensemble-averaged phase functions for equiprobable shape mixtures of polydisperse prolate spheroids with different aspect-ratio ranges, all centered on $\varepsilon = 1.8$. Panel (d) shows the phase functions for polydisperse spheres and ensemble-averaged phase functions for equiprobable shape mixtures of prolate spheroids (green curve), oblate spheroids (blue curve), and prolate and oblate spheroids together (red curve) with aspect ratios ranging from 1.2 to 2.4 in steps of 0.1. (After Mishchenko *et al.* 1997a.)

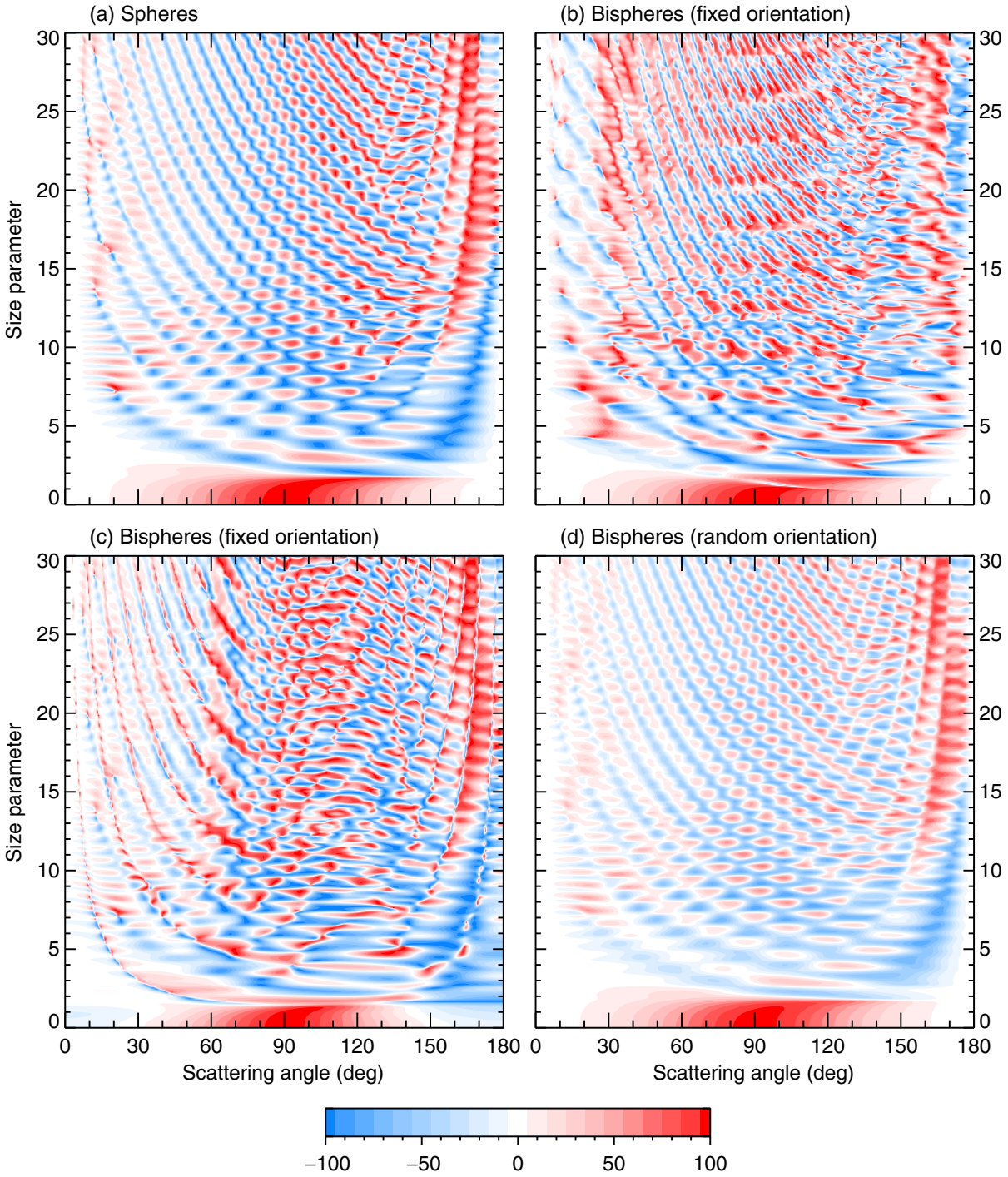


Plate 10.8. Panel (a): the ratio $-Z_{21}(\vartheta^{\text{sca}}, \varphi^{\text{sca}}=0; \vartheta^{\text{inc}}=0, \varphi^{\text{inc}}=0) / Z_{11}(\vartheta^{\text{sca}}, \varphi^{\text{sca}}=0; \vartheta^{\text{inc}}=0, \varphi^{\text{inc}}=0)$ in % versus ϑ^{sca} and size parameter for monodisperse single spheres. Panels (b)–(d): the same ratio versus ϑ^{sca} and constituent-sphere size parameter for monodisperse bispheres with equal touching components in fixed and random orientations. In panels (b) and (c) the bisphere axis is oriented respectively along the z -axis and along the x -axis of the laboratory reference frame. The relative refractive index is $1.5 + i0.005$.

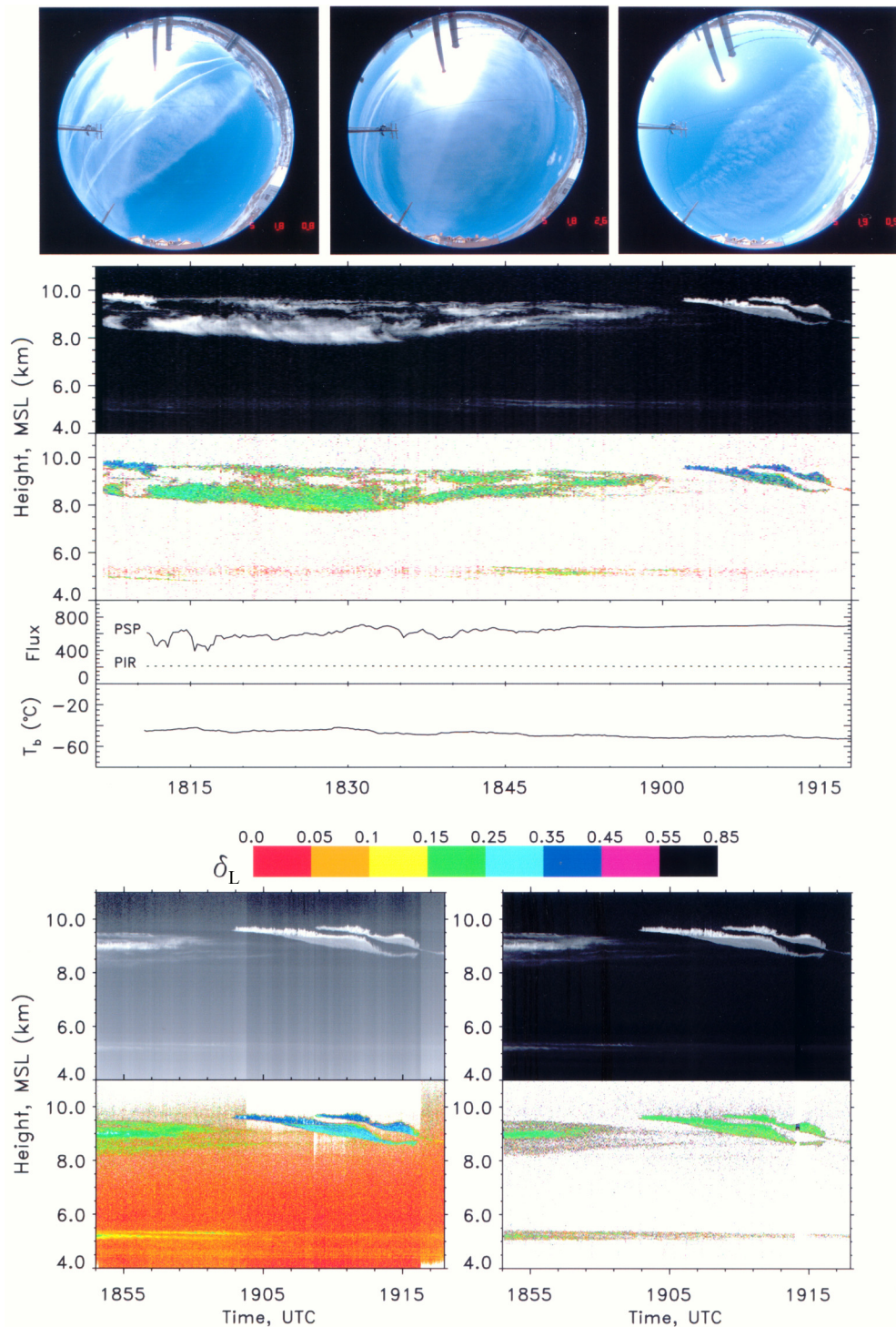


Plate 10.9. Compilation of data for the case study on 5 March 1999 of cirrus, contrails, and an Asian dust layer above Salt Lake City, Utah. Shown from top to bottom are: three fish-eye photographs of all-sky cloud conditions, obtained at 1808, 1826, and 1905 UTC (from left to right); backscattered intensity and linear depolarization time-height displays measured by an upward-looking lidar at a wavelength $0.694 \mu\text{m}$, the broadband visible and infrared hemispherical fluxes, and the mid-infrared column brightness temperatures T_b ; and, at the bottom, expanded views of backscattered intensity (black and white images) and linear depolarization (colored images) at wavelengths $0.532 \mu\text{m}$ (bottom left panel) and $1.06 \mu\text{m}$ (bottom right panel) for a time range near the end of the measurement period. The depolarization displays can be quantified using the inserted color bar. (From Sassen *et al.* 2001.)